RSC Advances

PAPER

View Article Online
View Journal | View Issue

Cite this: *RSC Adv.*, 2020, **10**, 15387

Biodegradable rare earth fluorochloride nanocrystals for phototheranostics†

Xinyu Zhao,‡[a] Qi Yu,‡[a] Jun Yuan,[b] Nitish V. Thakor[b] and Mei Chee Tan *[a]

Received 24th January 2020
Accepted 13th April 2020

DOI: 10.1039/d0ra00760a

rsc.li/rsc-advances

Rare earth (RE) doped inorganic nanocrystals have been demonstrated as efficient contrast agents for deep tissue shortwave-infrared (SWIR) imaging with high sensitivities leading to potential early detection of tumors. However, a potential concern is the unknown long-term toxicity and incompatibility of inorganic nanocrystals. In this work, biodegradable rare earth nanocrystals of Nd doped SrFCl coated with polydopamine (SrFCl:Nd@PDA) were designed. Instead of traditional fluoride hosts, the chlorinated SrF_2 (*i.e.* SrFCl) with low phonon energy which significantly improved the brightness of SrFCl:Nd in the SWIR region was used as the host. After coating with a NIR-absorptive PDA layer, the SrFCl:Nd nanoparticles serve as not only a contrast agent for photoacoustic imaging, but also a potential photothermal agent for cancer therapy. Moreover, these SrFCl:Nd@PDA nanoparticles can be rapidly and completely degraded in phosphate buffer solution within 1 h, which effectively addresses the concerns of the deleterious effects arising from potential long term accumulation. The increased accumulation and retention at tumor sites, and complete *in vivo* clearance ~6 h after injection make these SrFCl:Nd@PDA nanoparticles a promising degradable phototheranostic agent.

1. Introduction

Inorganic nanoparticles are widely investigated for therapeutic and diagnostic purposes in both preclinical and clinical phases as they offer numerous unique size-dependent physicochemical, magnetic (*e.g.*, superparamagnetic contrast agents) and optical properties (*e.g.*, quantum dots).[1–6] However, there are few instances where inorganic nanomaterials have been used in clinical applications. Unlike their organic or polymeric counterparts, the poor solubility of inorganic crystalline nanomaterials precludes their efficient clearance from the body. Specifically, inorganic nanoparticles are difficult to clear through the renal system, especially considering the relatively large hydrodynamic diameter (HD) after serum protein adsorption.[7,8] Long-term particle retention in the body (*i.e.*, mostly in reticuloendothelial system (RES) and lung) could pose severe and unpredictable toxicity risks and interfere with subsequent diagnostic testing and imaging (*e.g.* heavy metal nanoparticles like gold nanoparticles may preclude accurate computed tomographic (CT) scanning). Against this backdrop, developing inorganic agents with favorable clearance properties holds the key to their eventual clinic use. At present, the biodegradation of inorganic nanoparticles mainly involves dissolution under acidic conditions (*e.g.* calcium phosphate, iron oxide). However, the *in vivo* degradation rate of these inorganic nanoparticles is usually at least a couple of hours, depending on the initial particle size. Therefore, a faster degradation method would be highly desirable for inorganic nanoparticles to be useful for clinical biomedical imaging.

Here, we present a rapidly degrading, phototheranostic agent with capabilities for shortwave infrared (SWIR) and photoacoustic (PA) imaging and photothermal therapy. As shown in Scheme 1a, a fluorochloride host (*i.e.* SrFCl) was used to host the rare-earth (RE) dopant neodymium (Nd) to facilitate deep tissue shortwave infrared (SWIR) imaging. Compared to its fluoride counterpart (*e.g.* $NaYF_4$), SrFCl has lower phonon energy (*i.e.*, between fluoride and chloride) than fluorides, which favors high radiative efficiency and bright SWIR emissions.[9–11] More importantly, the likely dissolution of SrFCl NPs into Sr^{2+}, F^- and Cl^- ions in *in vivo* environment can potentially facilitate subsequent excretion through renal filtration, endowing our theranostic agent with fast degradation and complete renal clearance features. To improve the biocompatibility and dispersion of Nd doped SrFCl (SrFCl:Nd) NPs, the surfaces of nanoparticles were modified with the biocompatible

[a]*Engineering Product Development, Singapore University of Technology and Design, 8 Somapah Road, Singapore 487372. E-mail: meichee.tan@sutd.edu.sg*

[b]*Singapore Institute for Neurotechnology (SINAPSE), National University of Singapore, 28 Medical Drive, #05-COR, Singapore 117456*

† Electronic supplementary information (ESI) available: Additional data for characterization of our Nd doped SrFCl and SrF_2 nanoparticles, including the following: SEM image, steady-state and time-resolved luminescence spectra, integrated PL emission intensities and fitted decay time using single exponential fitting of SrFCl nanoparticles doped with varying Nd dopant concentration from 1 to 10 mol%; PL emission spectra and integrated emission intensities of $SrFCl:Nd_2$ and $SrF_2:Nd_2$ NPs. Additional data for characterization of $SrFCl:Nd_2$@PDA NPs, including TGA, FTIR, PA spectra and PA images. See DOI: 10.1039/d0ra00760a

‡ Authors contributed equally to this work.

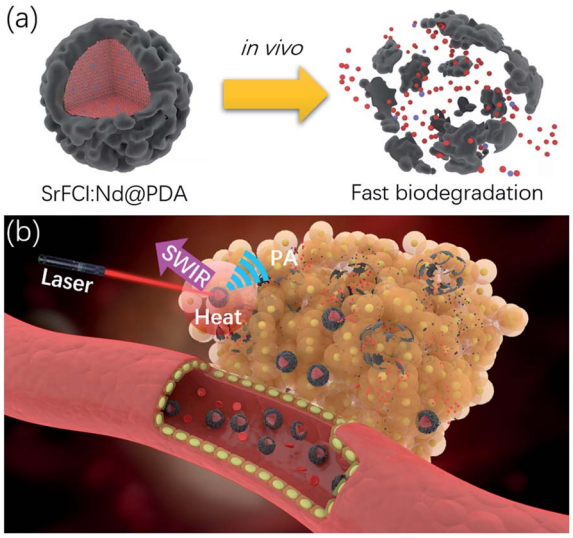

Scheme 1 (a) Schematic illustration of the core–shell structured SrFCl:Nd@PDA NPs before and after *in vivo* biodegradation. (b) Illustration of SrFCl:Nd@PDA NPs *in vivo* as a theranostic agent for dual modal imaging and photothermal therapy.

polydopamine (PDA),[12–14] which can be utilized as a PA imaging and photothermal agent through efficient near infrared absorption. As shown in Scheme 1b, we predicted that after SrFCl:Nd@PDA nanoparticles were injected in the mice model, they will accumulate tumor site *via* the enhanced permeability and retention (EPR) effect and give rise to a strong PA signal for improved imaging. Good photothermal conversion efficiency of SrFCl:Nd@PDA nanoparticles will result in significant localized temperature increase at the tumor site. Most importantly, the subsequent degradation of the SrFCl:Nd@PDA NPs will undergo self-clearance. The findings from this work on the design and synthesis of degradable inorganic nanomaterials presents a proof of concept of a new generation of multifunctional phototheranostic agents that are suitable for imaging and therapy, and at the same time conferring the benefit of rapid clearance *in vivo*.

2. Results and discussion

2.1. Bright SrFCl:Nd and SrFCl:Nd@PDA nanophosphors

Nd doped SrFCl nanoparticles (SrFCl:Nd NPs) were synthesized using a thermal decomposition method. It is evident based on the X-ray diffraction (Fig. 1a, grain size $\sim$ 35.4 $\pm$ 5.8 nm calculated using the Scherrer's equation) that the synthesized SrFCl are tetragonal. Scanning electron microscopy (SEM) image shows that plate-like SrFCl:Nd particles with nanometer scale thickness (*i.e.* 166 $\pm$ 25 nm $\times$ 185 $\pm$ 27 nm $\times$ 20 $\pm$ 7 nm) (Fig. S1a†) were synthesized. The steady state photoluminescence spectrum for SrFCl:Nd upon excitation at 808 nm shows the characteristic SWIR emission peaks at $\sim$1057 nm and $\sim$1331 nm that are attributed to the $^4F_{3/2} \rightarrow {}^4I_{11/2}$ and $^4F_{3/2} \rightarrow {}^4I_{13/2}$ transitions of the rare earth dopant, Nd^{3+} (Fig. S1b†).[15,16] In these degradable rare earth nanocrystals, Nd^{3+} ions serve as both the sensitizer and activator. They harvest 808 nm light and transfer the energy to the surrounding Nd^{3+} ions, which give rise to the strong SWIR emissions at $\sim$1057 and 1331 nm. To obtain bright SWIR emissions, sufficiently high dopant concentrations are needed to maximize the number of activators participating in the radiative process and for efficient sensitization *via* upper state energy transfer. However, the reduction of interionic distance at higher dopant concentrations leads to undesirable energy transfer or cross-relaxation processes, where preferential nonradiative relaxation occurs. This phenomenon of reducing emissions beyond a critical concentration is defined as concentration quenching. The optimum Nd concentration was determined as $\sim$2 mol% from steady-state luminescence measurements from a range of SrFCl:Nd NPs (Fig. 1b).

To evaluate the SWIR emission efficiency of as-synthesized SrFCl:Nd NPs, the time resolved emission spectra were measured (Fig. 1c). The luminescence decay curve was fitted using a single exponential equation of $I = I_0 \exp(-t/\tau)$, where I_0 is the initial emission intensity at $t = 0$ and τ is the fitted decay lifetime. The decay time of as-synthesized SrFCl:Nd_2 NPs was estimated to be $\sim$376 and $\sim$244 μs for the $^4F_{3/2} \rightarrow {}^4I_{11/2}$ ($\sim$1057 nm) and $^4F_{3/2} \rightarrow {}^4I_{13/2}$ ($\sim$1331 nm) transitions. The decay time characterizes the radiative and non-radiative relaxation processes of excited states. A long decay time indicates low non-radiative losses and high emission efficiency. Therefore, the longer decay time for the $\sim$1057 nm emission of $\sim$376 μs for our SrFCl:Nd_2 compared to the reported value of $\sim$175 μs for Nd doped $NaYF_4$ suggests that brightly SWIR emitting SrFCl:Nd_2 nanophosphors were successfully synthesized.[17] The longer decay time for the SrFCl:Nd_2 nanophosphors could be attributed to the lower phonon energy of fluorochloride hosts compared to its fluoride counterparts.[18] For non-radiative relaxation, since more phonons are needed in low phonon energy hosts to bridge the small energy gaps characteristic of infrared transitions, non-radiative losses are less likely leading to more efficient emissions (*i.e.* radiative transitions); making low phonon energy materials favored hosts for bright emissions. The measured emission spectra of SrFCl:Nd_2 NPs and SrF_2:Nd_2 NPs show that the integrated infrared emission intensity of SrFCl:Nd_2 NPs is $\sim$24, $\sim$17 and $\sim$22 times higher than that of SrF_2:Nd_2 NPs for the 1057 nm, 1331 nm and sum of both emission peaks, respectively (Fig. S1c and d†). This significant enhancement in emission was attributed to the lower phonon energy and larger crystal sizes of our SrFCl:Nd_2 NPs (35.4 $\pm$ 5.8 nm) compared to that of SrF_2:Nd_2 NPs (6.6 $\pm$ 0.9 nm).

The as-synthesized SrFCl NPs were coated with oleic acid molecules resulting in an undesirable hydrophobic surface. To utilize these nanoparticles for biomedical applications (*i.e.* aqueous environment), surface modification is essential to transform the originally hydrophobic surface to a hydrophilic one and therefore to limit the aggregation of SrFCl NPs within an aqueous environment. Biocompatible molecules are effective surfactant candidates for surface modification of oleic acid coated rare earth doped nanoparticles. In this work, polydopamine (PDA) was used as the surface coating layer to improve the dispersion and biocompatibility of SrFCl NPs in an *in vivo*

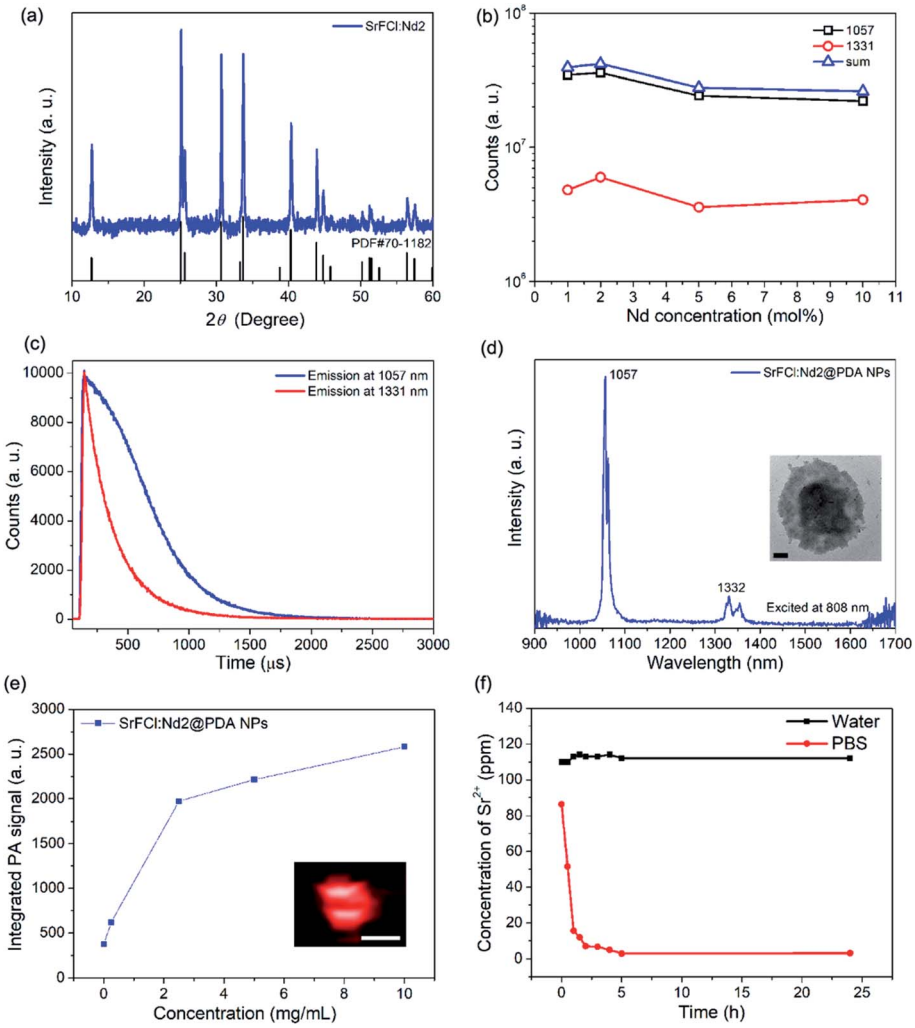

Fig. 1 (a) XRD pattern showing pure tetragonal SrFCl phase. (b) Integrated emission intensities at 1057 nm, 1331 nm and sum of both IR emissions for different Nd dopant concentrations show that the strongest emission was measured 2 mol%. (c) Time-resolved luminescence spectra of SrFCl:Nd_2 NPs for 1057 nm and 1331 nm emission. (d) SWIR emissions at 1057 and 1332 nm emissions are located within the second infrared tissue transparent window of 1000–1700 nm. Inset: TEM image showing the core–shell structure with a PDA shell thickness of ~68 nm (particle size ~ 323 nm). Scale bar: 50 nm. (e) Measured PA signals excited with the near infrared source. Inset: PA image of SrFCl:Nd_2@PDA NPs showing strong signals at 10 mg mL^{-1}. Scale bar: 1 mm. (f) Dissolution curve of SrFCl:Nd_2@PDA showing rapid degradation of inorganic nanocrystal in phosphate buffered saline (PBS) solution and water.

environment. Additionally, PDA can help to generate strong PA signals through efficient near infrared absorption, and to add a photothermal therapeutic function by efficiently converting absorbed light into heat. Successful PDA coating was validated based on the FTIR (Fig. S2a†) and TGA (Fig. S2b,† ~55 wt% PDA) results. The PDA coating improves the dispersity of our particles in polar solvents due to the substantive hydroxyl and amine groups of PDA molecules. TEM image shows that a uniform layer of PDA with the thickness of ~68 nm was successfully coated onto our SrFCl:Nd NPs (Fig. 1d inset). In addition, SWIR emissions from SrFCl:Nd_2@PDA were measured (Fig. 1d and S1†) to show that any undesired attenuation of the SWIR emissions was limited. The limited attenuation was attributed to the lack of overlap between SrFCl:Nd_2 emission and PDA absorption bands, where PDA exhibits a broad and featureless absorption ranging from below 900 nm (Fig. S2c†). *In vitro* PA measurements show that strong PA signals were measured from the SrFCl:Nd_2@PDA NPs upon NIR excitation from 680 to 970 nm (Fig. 1e and S3†). With increasing particle concentrations, the PA signal amplitude increases before plateauing when detector saturation is reached. The PA signal arising from the presence of the particles were likely generated from the non-radiative relaxation processes after preferential near infrared absorption by the Nd^{3+} ions (*i.e.*, 808 nm) and PDA coating (*i.e.*, <800 nm). The degradation of SrFCl:Nd_2@PDA NPs was next studied by evaluating its solubility in both pure water and phosphate buffered saline (PBS) solution with a pH at 7 (Fig. 1f). In both solutions, most of the SrFCl was shown to have dissolved within the first hour. In PBS, an insoluble precipitate was formed between Sr^{2+} and PO_4^{3-} leading to a drop in the Sr^{2+} ion concentration in solution.

Next, the *in vivo* distribution of SrFCl:Nd_2@PDA NPs was evaluated using a subcutaneous tumor-bearing mice. The SrFCl:Nd_2@PDA NPs were administered *via* intratumoral (*i.e.*, directly into the subcutaneous tumor) and intravenous injection routes, and the images of the nanoparticle distribution were captured at 0 h, 3 h, 6 h and 72 h post-injection. By administering the SrFCl:Nd_2@PDA NPs *via* intratumoral injection, a high particle concentration would be localized at the injection site. This was evident in Fig. 2, where a strong, localized PA signal was observed 0.5 h post intratumoral injection. At 3 h post intratumoral injection, the SrFCl:Nd_2@PDA NPs distributed uniformly throughout the tumor from the original point of injection. From ~6 h post intratumoral injection, the diminishing PA signals throughout the tumor suggest that most of the SrFCl:Nd_2@PDA had cleared from the tumor site. The clearance of the SrFCl:Nd_2@PDA was most likely facilitated by the degradation of SrFCl:Nd_2 in the aqueous environment. It should be noted that PA signals could still be measured from a small region at the injection site. This was possibly due to the presence of residual SrFCl:Nd_2@PDA that did not enter the systemic circulation during injection and had instead diffused into the extracellular matrix of the tumor.

In contrast, SrFCl:Nd_2@PDA that were administered *via* intravenous injection showed complete clearance after ~6 h. At 0.5 h and 3 h post intravenous injection, a uniform PA signal was observed at the tumor site suggesting uniform distribution and localization of SrFCl:Nd_2@PDA NPs. The absence of PA signals at the tumor site after ~6 h post intravenous injection indicate that the SrFCl:Nd_2@PDA were rapidly cleared. The rapid *in vivo* clearance was most likely facilitated by the degradation of SrFCl:Nd_2 in the aqueous environment. Compared to our previous studies where particle clearance from the tumor site was typically observed between 2 to 3 days using much smaller fluoride nanocrystals,[5,6,19] the much faster clearance of the much larger SrFCl:Nd_2@PDA within 12 h post injection suggests that the solubilization of SrFCl was instrumental towards the rapid inorganic nanocrystal clearance. The strong PA signal after intravenous injection coupled with complete clearance at 6 h after injection shows that SrFCl:Nd_2@PDA NPs is a suitable PA imaging diagnostic agent.

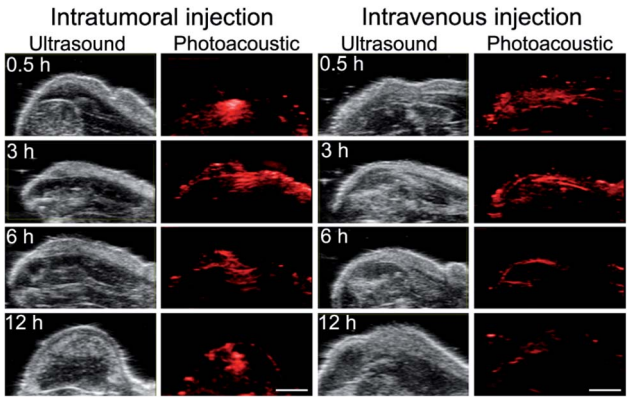

Fig. 2 *In vivo* PA images taken at different time points showing the distribution and clearance or degradation of SrFCl:Nd_2@PDA NPs that were administered *via* intratumoral or intravenous injection routes. Scale bar represents 2 mm.

To further investigate of the possibility of using SrFCl:Nd_2@PDA NPs as a photothermal therapy agent, the photothermal effects in tumor-bearing nude mice were analyzed using an IR thermal mapping camera (Fig. 3). The temperature of the tumor region was monitored under 808 nm laser irradiation (0.4 W cm^{-2}) after injection of SrFCl:Nd_2@PDA NPs both intratumorally and intravenously. A marked increase in temperature of ~13 °C at the irradiated tumor site (spot 1) after intravenous or intratumoral administration of the particles was observed in comparison with unexposed tissue (spot 2). For PT therapeutic applications, the range of therapy temperature is normally lower than 50 °C to reduce undesired inflammation and cell necrosis to protect healthy cells from the high temperature surrounding.[20,21] Moderate therapy temperatures ranging from 43 to 45 °C have been reported to be adequate in inducing cell death by activating all apoptotic pathways.[20,21] Therefore, the measured ~13 °C temperature increase indicates that these multifunctional SrFCl:Nd_2@PDA imaging contrast agents could also serve as potential phototherapeutic agents that initiate localized cell death with minimal injury to the surrounding tissues.

3. Summary

In summary, we have designed Nd doped SrFCl nanoparticles (SrFCl:Nd NPs) coated with polydopamine (PDA) with excellent biodegradability for SWIR and photoacoustic (PA) dual-modal imaging and photothermal therapy. SrFCl:Nd NPs have shown enhanced SWIR emission (*i.e.* 1057 nm and 1331 emission) compared to their fluoride counterpart (SrF_2:Nd NPs) due to the intrinsic lower phonon energy of fluorochloride. The surface modification of SrFCl:Nd NPs with a versatile, biocompatible polydopamine (PDA) coating further enhances the infrared absorption properties of our contrast agent to enable PA imaging and photothermal therapy. Furthermore, the PDA coating facilitates increased accumulation and retention at the tumor site as evident by the localized enhancement of PA signal intensities. The excellent biodegradability SrFCl:Nd_2@PDA was apparent from a complete clearance at the tumor site after a short period of ~6 h after either intratumoral or intravenous injection. Therefore, our SrFCl:Nd_2@PDA NPs with enhanced SWIR emission and PA signal, excellent biodegradability and good photothermal therapy ability hold great potential for phototheranostic applications.

4. Experimental section

4.1. Materials

Strontium carbonate ($SrCO_3$, 99.9%), neodymium(III) oxide (Nd_2O_3, 99.9%), 1-octadecene (ODE, 90%), oleic acid (OA, 90%), trifluoroacetic acid (TFA, 99%), trichloroacetic acid (TCA, 99%), ammonium hydroxide solution (28–30% in H_2O), and dopamine hydrochloride were purchased from Sigma-Aldrich (Sigma-Aldrich, St. Louis, MO). Hexane (95%), ethanol (95% with 5% methanol) and isopropanol (IPA, 99.7%) were

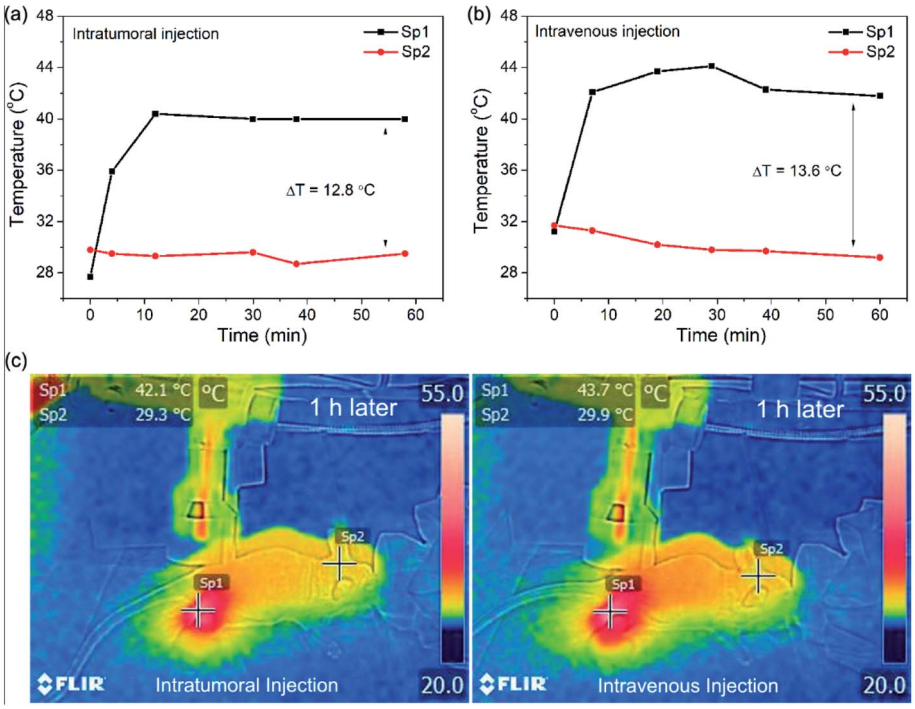

Fig. 3 Increase in local temperature observed for SrFCl:Nd_2@PDA NPs that were administered intravenously or directly to the tumor *via* intratumoral injection. Infrared (IR) thermographs at different time points for tumor-bearing mice, where only the tumor was directly exposed to the 808 nm source with a power density of 0.4 W cm^{-2}. The temperature profiles were monitored for ~60 min at the tumor site (spot 1, sp1) and normal site (spot 2, sp2) of the mice that were administered with the particles either by intravenous or intratumoral injection.

purchased from Aik Moh (Aik Moh Chemicals, SG). All chemicals were used as received without any further purification.

4.2. Synthesis of SrFCl:Nd nanoparticles

The Nd doped SrFCl nanoparticles were synthesized using a one-pot thermal decomposition method. Strontium and neodymium trifluoroacetate precursors were prepared by dissolving strontium carbonate or neodymium oxide in trifluoroacetic acid at room temperature or 80 °C. In a typical experiment, 0.98 mmol $Sr(CF_3COO)_2$, 0.02 mmol $Nd(CF_3COO)_3$ and 1 mmol trichloroacetic acid (TCA) were dissolved in a solution of 5 mL oleic acid and 5 mL 1-octadecene in a 100 mL three-neck flask and then the solution was degassed by vacuum for 15 min at 100 °C under vigorous stirring. Next, the solution was rapidly heated to 280 °C and maintained for 1 h in an argon (Ar) environment. The mixture of as-synthesized NPs was cooled to room temperature and precipitated using ethanol, before being washed several times using centrifugation.

4.3. Synthesis of SrF_2:Nd nanoparticles

In a typical experiment, 0.98 mmol $Sr(CF_3COO)_2$ and 0.02 mmol $Nd(CF_3COO)_3$ were dissolved in 10 mL oleic acid in a 100 mL three-neck flask and then the solution was degassed by vacuum for 15 min at 100 °C under vigorous stirring. Next, the solution was rapidly heated to 330 °C and maintained for 1 h in an argon (Ar) environment. The mixture of as-synthesized NPs was cooled to room temperature and precipitated using ethanol, before being washed several times using centrifugation.

4.4. Polydopamine (PDA) coating

Polydopamine (PDA) coating was conducted using a modified reported method in isopropanol solution. In a typical experiment, 10 mg SrFCl nanoparticles were redispersed in 15 mL of 1 mg mL^{-1} dopamine HCl in isopropanol. The reaction was vigorously stirred and 0.25 mL of aqueous NH_4OH was added. The reaction was allowed to stir for 6 h. The PDA coated nanoparticles were precipitated by centrifugation and washed for three times using IPA to remove residual reagents.

4.5. Measuring PA properties of nanoparticles *in vitro*

The as-synthesized nanoparticles were dispersed in distilled water at 10, 5, 2.5, and 0.25 mg mL^{-1}, vortexed and sonicated for 1 min. 0.2 mL of dispersed nanoparticles was injected by a 1 mL syringe and 27 gage needle into contrast agent phantom tubing (Vevo, Fujifilm VisualSonics, Canada), which was secured on PHANTOM imaging chamber (Vevo). Near infrared PA measurements, using a light source covering 680–970 nm, were performed using Vevo Lazr-X imaging platform (Vevo). The images were acquired and analyzed by Vevo® LAB.

4.6. Measuring PT and PA properties of nanoparticles *in vivo*

The mouse tumor model was established with T-cell deficient nude mice (CrTac:NCr-Foxn1nu, InVivos, Singapore) and mouse

breast tumor cell line 4T1 (CRL-2539™, ATCC®, VA). 4T1 cells were cultured with medium RPMI-1640 Medium (30-2001™, ATCC®, VA) supplemented with 10% FBS (S1810, Biowest, France) and 100 IU mL^{-1} penicillin–100 μg mL^{-1} strep (SV30010, GE Healthcare, Singapore). 0.5×10^6 of 4T1 cells were next harvested from culture flasks, for subcutaneous implantation into the leg of nude mice and incubated for 5–7 days. Mice were monitored daily for tumor growth and size changes.

For conducting *in vivo* PA measurements and PT for a subcutaneous breast tumor model, mice were first anesthetized with isoflurane and next secured on a stage. For PT measurements, the 808 nm laser source with an estimated beam size of ~0.785 cm^2 and power density of 0.4 W cm^{-2} was focused on the tumor site. The temperature change during the irradiation was measured by a thermographic camera (FLIR E40, NC). For PA imaging using the Vevo Lazr-X imaging platform (Vevo, Fujifilm VisualSonics, Canada), the near infrared PA signals at tumor sites were measured. The images were acquired and analyzed by the instrument's software. Freshly prepared nanoparticles dispersed in distilled water were subsequently injected at 10 mg kg^{-1} both intratumorally (30 μL) and intravenously (100 μL). PA imaging at the tumor site was conducted at 3, 6 and 72 h post injection to monitor nanoparticle distribution. PT measurements were used to monitor the temperature of the mice immediately after intratumoral and intravenous injection. All experiments were performed in accordance with the approved guidelines and regulations, and were approved by the Institutional Animal Care and Use Committee of the National University of Singapore. The animals were housed at a constant temperature and humidity with free access to food and water.

4.7. Material characterization

X-ray powder diffraction (XRD) patterns were measured with a D8 Eco Advance powder diffractometer (Bruker AXS, Madison, WI) using Cu-Kα radiation of 1.54 Å (0.02° per step, 0.5 s per step, 40 kV, 25 mA). Reference powder diffraction files of tetragonal SrFCl from JCPDS 70-1182 was used to identify the phase of as-synthesized particles. Particle size and morphology was observed using field emission scanning electron microscope (JSM-7600F, JEOL, JP.) operating at 5 kV, with 6 mA probe current and working distance of 4.2 mm. The steady-state emission spectra were measured using a FLS980 spectrometer (Edinburgh Instruments, UK) with a 2 nm step size and 0.2 s dwell time, upon excitation of powder samples from a continuous wave laser (Changchun New Industries Optoelectronics Tech, China). The powder samples were packed in demountable Spectrosil Type 20 cell (Starna Cells, Atascadero, CA) with a 0.5 mm path length. To measure the time-resolved luminescence spectrum, the excitation source was modulated using an electronic pulse modulator to obtain excitation pulse at pulse duration of 30 μs with a repetition rate of 10 Hz. The amounts of Sr^{2+} present in solution after dissolving the as-synthesized powders were measured using the inductively coupled plasma method. Typically, an aliquot of the supernatant was collected after solubilizing a fixed mass of powder samples in 20 mL of water. The amount of Sr^{2+} in the supernatant was quantified using Inductively Coupled Plasma-Optical Emission Spectrometer (ICP-OES, PerkinElmer, Optima 5300DV, Waltham, MA). Count rates for Sr was correlated using a standard curve generated with 0.01, 1, 10, 100 ppm Sr standard solutions.

Conflicts of interest

There are no conflicts to declare.

Acknowledgements

M. C. T. and X. Z. would like to gratefully acknowledge the funding support from the A*STAR AME Individual Research Grant (reference number: A1883c0015). M. C. T. and Q. Y. also acknowledge the support from the National Institute of Health/National Institute of Biomedical Imaging and Bioengineering (2 R01 EB018378-05). J. Y. and N. V. T. would also like to thank the support from the National Research Foundation Competitive Research Program (R719-000-017-281 and R719-000-018-281).

References

1 L. Prodi, E. Rampazzo, F. Rastrelli, A. Speghini and N. Zaccheroni, *Chem. Soc. Rev.*, 2015, **44**, 4922–4952.
2 Y. Sheng, L. De Liao, N. V. Thakor and M. C. Tan, *J. Biomed. Nanotechnol.*, 2014, **10**, 2641–2676.
3 F. Wang, D. Banerjee, Y. Liu, X. Chen and X. Liu, *Analyst*, 2010, **135**, 1839–1854.
4 X. Zhao, S. He and M. C. Tan, *J. Mater. Chem. B*, 2017, **5**, 4266–4275.
5 Z. Zhao, J. Yuan, X. Zhao, A. Bandla, N. V. Thakor and M. C. Tan, *ACS Biomater. Sci. Eng.*, 2019, **5**, 4089–4101.
6 Y. Sheng, L. D. Liao, N. Thakor and M. C. Tan, *Sci. Rep.*, 2014, **4**, 6562.
7 M. Longmire, P. L. Choyke and H. Kobayashi, *Nanomedicine*, 2008, **3**, 703–717.
8 H. S. Choi, W. Liu, P. Misra, E. Tanaka, J. P. Zimmer, B. I. Ipe, M. G. Bawendi and J. V. Frangioni, *Nat. Biotechnol.*, 2007, **25**, 1165–1170.
9 X. Chen, W. Zhao, R. Cook and G. Liu, *Phys. Rev. B: Condens. Matter Mater. Phys.*, 2004, **70**, 205122.
10 D. Chen, Y. Yu, F. Huang, P. Huang, A. Yang, Z. Wang and Y. Wang, *Chem. Commun.*, 2011, **47**, 11083–11085.
11 K. T. Dissanayake and F. A. Rabuffetti, *J. Mater. Chem. C*, 2016, **4**, 2447–2451.
12 J. H. Ryu, P. B. Messersmith and H. Lee, *ACS Appl. Mater. Interfaces*, 2018, **10**, 7523–7540.
13 S. H. Ku and C. B. Park, *Biomaterials*, 2010, **31**, 9431–9437.
14 S. H. Ku, J. Ryu, S. K. Hong, H. Lee and C. B. Park, *Biomaterials*, 2010, **31**, 2535–2541.
15 M. C. Tan, G. A. Kumar, R. E. Riman, M. G. Brik, E. Brown and U. Hommerich, *J. Appl. Phys.*, 2009, **106**, 063118.
16 X. Feng, R. Li, L. Wang, S. W. Ng, G. Qin and L. Ma, *CrystEngComm*, 2015, **15**, 7878–7887.
17 L. Marciniak, A. Pilch, S. Arabasz, D. Jin and A. Bednarkiewicz, *Nanoscale*, 2017, **9**, 8288–8297.

18 X. Feng, Y. Shang, H. Zhang, R. Li, W. Wang, D. Zhang, L. Wang and Z. Li, *RSC Adv.*, 2019, **9**, 16328–16338.
19 D. Naczynski, M. Tan, M. Zevon, B. Wall, J. Kohl, A. Kulesa, S. Chen, C. Roth, R. Riman and P. Moghe, *Nat. Commun.*, 2013, **4**, 2199.
20 Y. Zhang, X. Zhan, J. Xiong, S. Peng, W. Huang, R. Joshi, Y. Cai, Y. Liu, R. Li, K. Yuan, N. Zhou and W. Min, *Sci. Rep.*, 2018, **8**, 8720.
21 T. Mantso, S. Vasileiadis, I. Anestopoulos, G. P. Voulgaridou, E. Lampri, S. Botaitis, E. N. Kontomanolis, C. Simopoulos, G. Goussetis, R. Franco, K. Chlichlia, A. Pappa and M. I. Panayiotidis, *Sci. Rep.*, 2018, **8**, 10724.